Accepted Manuscript

Phosphorus, nitrogen and oxygen co-doped polymer-based core-shell carbon sphere for high-performance hybrid supercapacitors

Congcong Huang, Alexander M. Puziy, Olga I. Poddubnaya, Denisa Hulicova-Jurcakova, Magdalena Sobiesiak, Barbara Gawdzik

PII: S0013-4686(18)30419-5

DOI: 10.1016/j.electacta.2018.02.115

Reference: EA 31310

To appear in: *Electrochimica Acta*

Received Date: 9 November 2017

Revised Date: 20 February 2018

Accepted Date: 21 February 2018

Please cite this article as: C. Huang, A.M. Puziy, O.I. Poddubnaya, D. Hulicova-Jurcakova, M. Sobiesiak, B. Gawdzik, Phosphorus, nitrogen and oxygen co-doped polymer-based core-shell carbon sphere for high-performance hybrid supercapacitors, *Electrochimica Acta* (2018), doi: 10.1016/j.electacta.2018.02.115.

Phosphorus, Nitrogen and Oxygen co-doped Polymer-based Core-shell Carbon Sphere for High-performance Hybrid Supercapacitors

Congcong Huang [a*], Alexander M. Puziy [b*], Olga I. Poddubnaya [b], Denisa Hulicova-Jurcakova [c] ‡, Magdalena Sobiesiak [d], Barbara Gawdzik [d]

[a] Department of Food Engineering, Shandong Business Institute, Yantai 264670, China

[b] Institute for Sorption and Problems of Endoecology, National Academy of Sciences of Ukraine, Kyiv 03164, Ukraine

[c] School of Chemical Engineering and Australian Institute for Bioengineering and Nanotechnology, The University of Queensland, St Lucia, QLD 4072, Australia

[d] Maria Curie-Skłodowska University, Lublin 20-031, Poland

* Corresponding authors. E-mail: meiyueqinghe@163.com (Congcong Huang), alexander.puziy@gmail.com (Alexander M. Puziy)

‡Deceased October 2014

Highlights

> A series of oxygen, nitrogen and phosphorus co-doped core-shell carbon sphere were developed.

> The sample prepared at 800 °C with H_3PO_4 activation showed the highest capacity and energy density.

>The surface chemistry together with the well balanced porous structure of carbon electrode can greatly influence the electrochemical performance.

> The co-doped carbon can be used as promising materials for supercapacitors especially for the devices with high power density demand.

Keywords:

Co-doped carbon; Supercapacitors; Core-shell Carbon Sphere; Phosphoric acid activation

Abstract

Co-doping heteroatoms of the carbon lattice has been proven as an efficient strategy that can improve the capacitive performance, due to the synergetic effect of several dopants. Herein, a series of phosphorus, nitrogen and oxygen, co-doped polymer-based carbon spheres were prepared by the suspension polymerization method and chemical activation with phosphoric acid at different temperatures. The presence of heteroatoms was confirmed by X-ray photoelectron spectroscopy and elemental analysis. The structure of the carbons was characterized by scanning electron microscopy, Raman spectroscopy and nitrogen adsorption. Carbon obtained at 800 °C with a P, N and O doping level of 11.17 at%, 2.79 at% and 11.77 at% respectively, shows a capacitance of 157 F g^{-1} at the current density of 0.05 A g^{-1}. Moreover, the electrode can survive at a wide potential window of 1.5 V with only 15% decrease in capacity after 10000 cycles at a current density of 5 A g^{-1}, providing a high energy density of 10 Wh kg^{-1} and a high power density of 750 W kg^{-1}. For the outstanding features, it is expected that the phosphorus, nitrogen and oxygen co-doped carbons will be a very suitable material not only for supercapacitors, but also for lithium batteries and oxygen reduction reaction. In addition, the co-doping method described here might be extended to the preparation of other kinds of porous carbon materials.

1. Introduction

Carbon-based materials are the most promising electrodes for supercapacitors (SCs) due to large surface area, they are easy modifiable and are of low cost. However, the energy densities of carbon-based SCs fall far behind the ideal values, hampering their practical use. Therefore, there is ever increasing interest in improving the energy density without sacrifice the power density of the SCs. Due to the complex surface chemistry of carbon materials, normally, two kind of energy storage mechanisms coexist in carbon electrode, one involves accumulation of ionic charges on the double-layer between the electrode and the electrolyte, the other mechanism is fast Faradic redox reactions involving surface functional groups. By combining these two charge storage mechanisms, such SCs also can be called hybrid supercapacitors (HSCs).

According to the recent studies [1-5], heteroatomic functional groups on the surface of the carbon material have proven to increase the performance of the carbon based SCs in the way of contributing some pseudocapacitance as well as increase the surface wettability. One of the most common oxygen-containing functional group, quinone/hydroquinone, is involved in the reversible redox reaction that can contribute to Faradic pseudocapacitance (Fig. 1) [2]. Moreover, a Faradic reactions are thought to occur among the protons, the free electrons and the nitrogen in the carbon

matrix [1], as shown in Fig. 1. However, abundant nitrogen and oxygen functional groups on the surface of the carbon materials can lead to a poor cycling stability and large capacitance attenuation under the high current load of the SCs [6]. Furthermore, phosphorus is well known as one of the flame retardant element. If some phosphorus functional groups can be present in the carbon lattice at the same time, it will inhibit the occurrence of certain side effects, such as oxidation of carbon electrode [5, 7, 8], thus increasing the potential operation window, cycle stability and energy density of the SCs. In this respect, functionalization of carbonaceous materials with heteroatoms, such as phosphorus [5, 8], nitrogen [9, 10], boron [11], sulphur [12] and dual heteroatom co-doped carbon materials [13-15] have been recently studied as electrode in SCs.

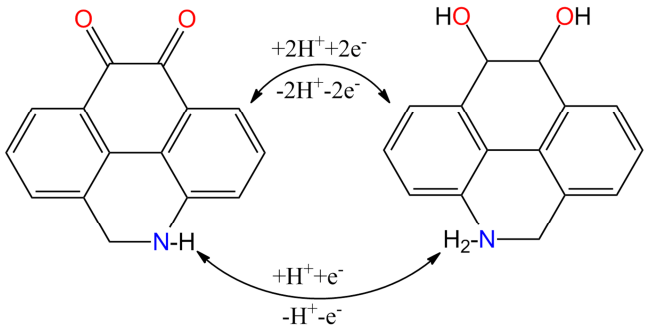

Fig. 1. Redox reaction of the oxygen and nitrogen functionalities on the carbon surface.

Besides the surface chemistry, the porous structure of carbon electrode can also greatly influence the electrochemical performance of the SCs. It has been reported [16] that the well designed three-dimensional (3D) porous carbon with a core-shell structure is beneficial to the electrochemical performance, because of the interconnected macropores, mesopores and micropores played the role of ion buffer, ion transport channels, and the charge adsorption carrier, respectively [17]. Such unique carbon skeleton can improve the ion channels of the carbon material, promote the transportation of electrolyte ions and increase the contact area between the active material and electrolyte [18], therefore, the assembled SCs has an excellent capacitive performance. In this aspect, many efforts have been devoted to design 3D porous carbons for SCs [19-21] to improve the kinetics issues.

Thus, the design of carbon electrode that combines heteroatom-doped surface chemistry with 3D architecture may have a great potential for fabrication of advanced HSCs.

Polyimide is a polymer of imide monomers. Polyimides have wide operating temperature, high chemical corrosion resistance, good dielectric properties and high mechanical strength. As one kind of special engineering material, it has been widely used in microelectronics [22], aviation [23], catalyst materials [24] and gas separation membranes [25]. Polyimides are considered as good precursor for preparation of carbon materials. The most important advantages of polyimides are the high yield and the absence of deformation during carbonization [26]. Previous studies have shown that highly porous spherically shaped carbon having large amount of acid surface groups can be obtained by phosphoric acid activation of polyimide copolymer [27-30]. However, phosphorus, oxygen and nitrogen co-doped polyimide-based carbons has yet to be investigated as electrodes in SCs.

Herein, by using nitrogen-enriched polyimide as the carbon precursor, phosphoric acid as the activating agent and phosphorus source, a series of phosphorus, nitrogen and oxygen co-doped

carbons were derived at different activation temperatures, which were expected to show some excellent electrochemical performances when used as the electrodes in SCs.

2. Experimental

2.1 Materials synthesis

Copolymer of 4,4'-bis(maleimidodiphenyl)methane (50 mol%) and divinylbenzene (50 mol%) (BM-DVB) was prepared by the suspension polymerization method using mixture of 1-decanol and benzyl alcohol as pore forming agents [28]. BM-DVB was first impregnated with 60% phosphoric acid (impregnation ratio 1.1), dried in air and then carbonized at different temperatures (400-1000 °C) in argon flow (0.5 L min^{-1}) for 30 min (Scheme 1). The obtained carbons were extensively washed with hot water in Soxhlet extractor until neutral pH, followed by drying at 110 °C. Carbons were abbreviated as PXXX where XXX stands for carbonization temperature. For example, P400 corresponds to carbon obtained at 400 °C. For comparison purpose, a carbon C800 was obtained by carbonization of the same copolymer precursor at 800 °C without impregnation with phosphoric acid.

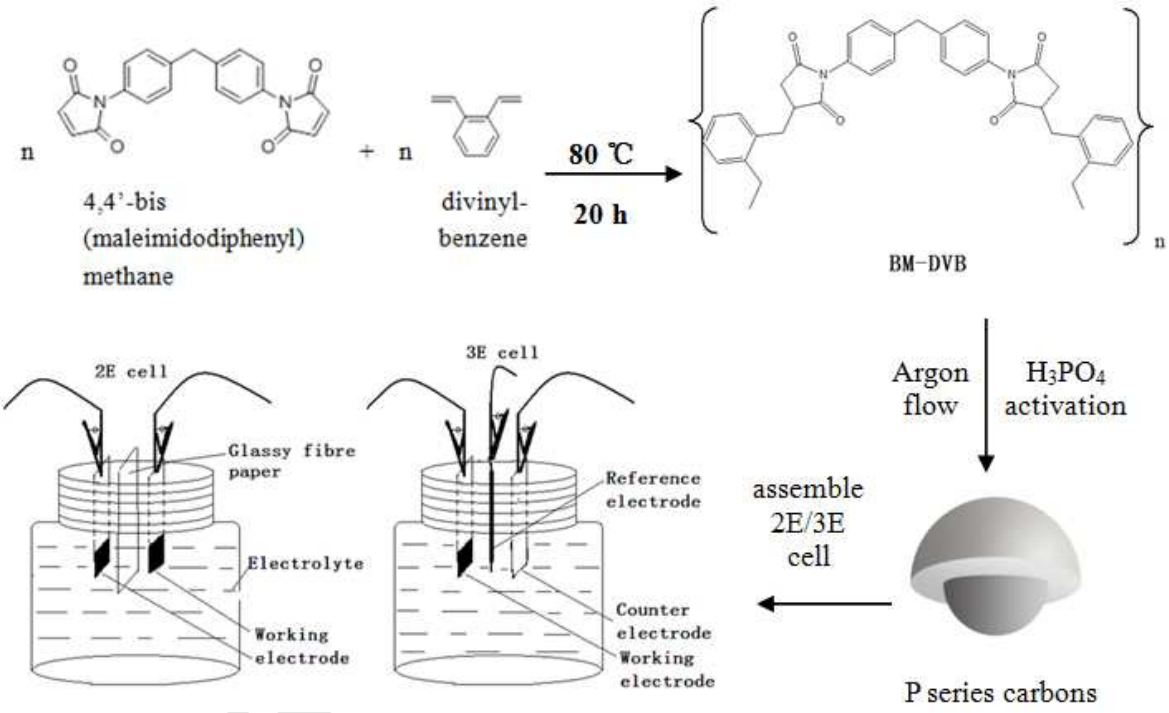

Scheme 1. Reaction formula of the BM-DVB copolymer, schematic illustration of the structure of P-carbons and assembly of 2E/3E cell.

2.2 Structural Characterization

Morphological characterization

The morphologies of the obtained carbons were characterized by a JSM-6300 (JEOL, Japan) scanning electron microscope (SEM) equipped with field emission gun. The sample chamber was evacuated to 8×10^{-5} mbar with an electron accelerating potential of 5-30 kV.

Structural defect measurement

A micro-Raman spectrometer (INVIA RENISHAW, UK) with 514 nm Ar^{+} excitation source was employed. Laser power was 10 mW and data acquisition time was 100 s, the recorded wavenumbers ranged from 500 to 3500 cm^{-1}.

Raman spectra were fitted with five peaks as described elsewhere [31]. I_D/I_G ratio was calculated as area ratio of fitted D and G peaks. Aromatic cluster diameter, La, was calculated as $La=(I_D/I_G/0.0055)^{-½}/10$ [32].

Determination of pore structure

The pore structure of all carbon samples was analysed by the N_2 adsorption measured at −196 °C using an ASAP 2010 (Micromeritics, USA) instrument. Prior to each measurement, samples were degassed at 250 °C overnight under vacuum. Surface area, S_{BET}, was calculated by Brunauer-Emmett-Teller (BET) method from N_2 sorption, micropore volume, V_{micro}, from N_2 sorption and from CO_2 sorption was calculated using Dubinin-Radushkevich (DR) method. Pore size distributions (PSD) were estimated from N_2 adsorption isotherms using the DFT Plus Software (Micromeritics, USA) by using the non-local density functional theory (NLDFT) method [33].

2.3 Surface Chemistry Characterization

Elemental analysis

Elemental analysis was done by a conventional combustion method by using FLASH EA 1112 instrument (Thermo Fisher, USA); it can detect the weight percentage of C, H, N, O in the bulk carbons. 2,5-bis(*tert*-butyl-2-benzoxazolyl)thiophene was selected as the standard substance, and the furnace temperature up to 900 °C under an oxygen flow (250 mL min^{-1}).

Surface characterization

The X-ray photoelectron spectroscopy (XPS) measurements were carried out on ESCALAB220i-XL (VG Scientific, UK) with an Al Kα X-ray source. The spectra were calibrated for a carbon C1s excitation at binding energy of 284.6 eV and taken as an internal standard. The quantitative analysis was performed with CASA XPS software after Shirley background subtraction. The best peak fits were obtained using mixed 30% Gaussian–Lorentzian line shapes with the same full width at half-maximum values for all fitted peaks.

2.4 Electrochemical measurements and calculations

The capacitive performance of carbon samples was tested in 1 mol L^{-1} H_2SO_4 electrolyte using both 2-electrode (2E) and 3-electrode (3E) cells. In electrode preparation, a mixture of 90 wt% carbon, 5 wt% poly(vinylidene fluoride) and 5 wt% of carbon black was dispersed in *N*-methyl pyrrolidone, then painted on a titanium foil (current collector) with total area of 1×1 cm^2, typically 2-4 mg of carbon was applied to each electrode. After drying at 100 °C for 24 h in a vacuum oven, two weighted electrodes were constructed by facing each other and separating with glassy fibre paper to assemble 2E cell. 3E cell was assembled by choosing one carbon electrode as working electrode, the other one as the counter electrode, and adding an Ag/AgCl/3M KCl electrode as the reference electrode (as shown in Scheme 1). 1 mol L^{-1} H_2SO_4 electrolyte was added to the cell under vacuum to reduce air contamination and improve wettability of the electrodes. The ac impedance of the capacitor cells was measured at a potential amplitude of 10 mV in a frequency range of 0.01 kHz to 100 kHz by using Solartron 1255B frequency response analyser. Both cyclic voltammetry (CV) measurements and galvanostatic charge/discharge (GC) tests were conducted using a Solartron 1480 Multistat station.

The single electrode specific capacitances (C_{single}) in 2E cell of the electrode materials were calculated by the following equation:

$$C_{cell-g}(F\ g^{-1}) = \frac{I(A)\times\Delta t(s)}{\sum m(g)\times\Delta U(V)} \qquad (1)$$

$$C_{single}(F\ g^{-1}) = 4\times C_{cell-g} \qquad (2)$$

where I, in Amperes, is the current load of the active material in the working electrode, Δt, in seconds, is discharge time, Σ_m, in grams, is the total weight of active material in both electrodes and ΔU, in Volts, is the potential difference in discharge process after omitting any iR drop. The energy density (*E*) and power density (*P*) were calculated according to Equation (3) and (4):

$$E(Wh\ kg^{-1}) = \frac{1}{2}C_{cell-g}\times\Delta U^2(V)/3.6 \qquad (3)$$

$$P(Wk\ g^{-1}) = \frac{1}{2}\frac{I(A)\times\Delta U(V)}{\sum m(kg)} \qquad (4)$$

3. Results and discussion

3.1 Morphology characterization

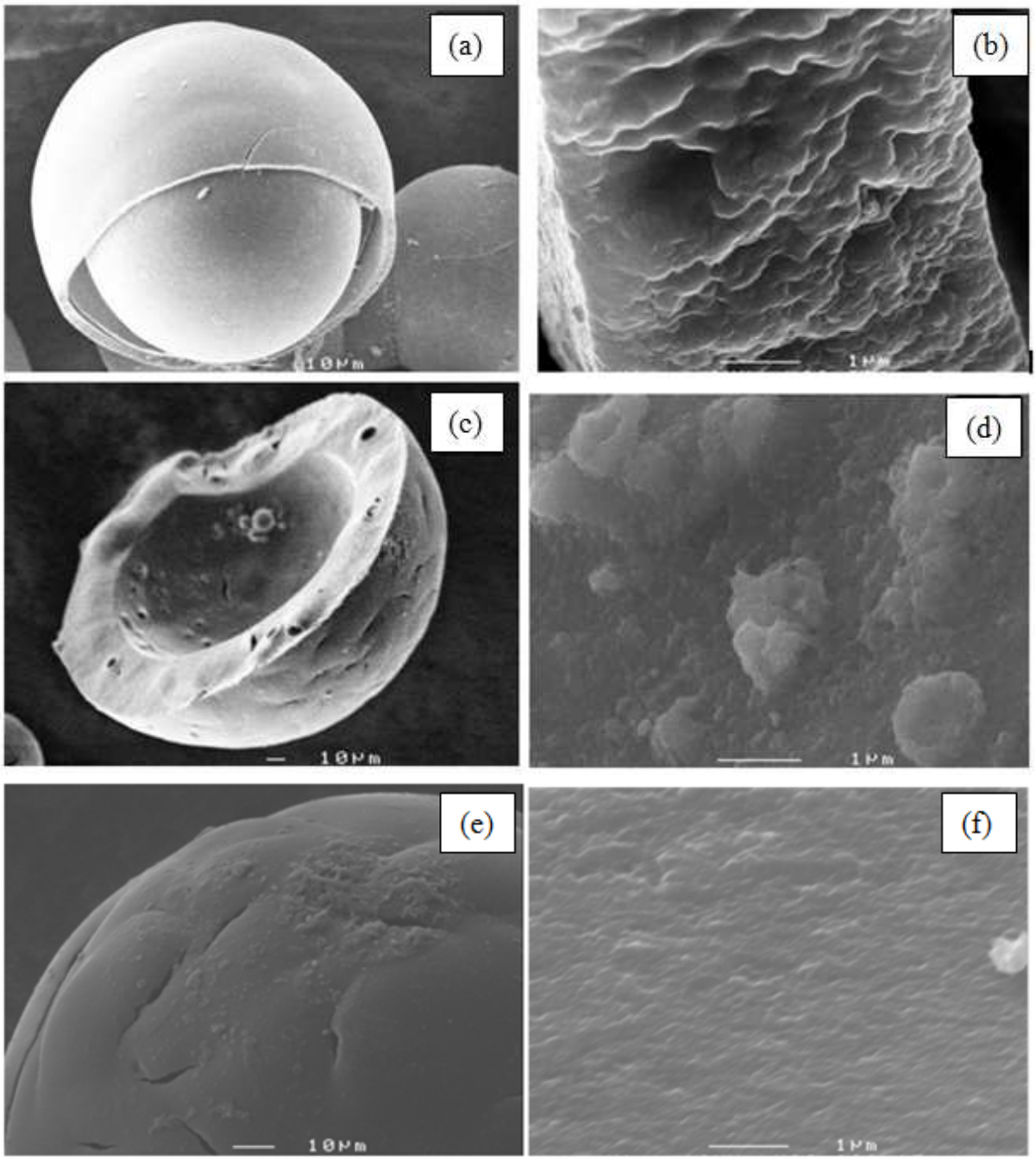

Fig.2. (a-b) SEM images of P400, (c-d) SEM images of P800, (e-f) SEM image of C800.

Figure 2 shows SEM images of co-doped polyimide carbon spheres obtained at low (400 °C) and high activation temperatures (800 °C). At low-magnification (Fig. 2 a), the morphology of P400 is represented by carbon spheres with a core-shell structure which diameter is around 100 μm. From Fig. 2 b it can be observed that P400 shows the smooth surface with a shell of 5 μm thick at high-magnification. It can be concluded that the absence of porosity in carbon P400 (see Subsection 3.3) is caused by the insufficient activation with phosphoric acid at 400 °C. By contrast, P800,

which is obtained at high activation temperature of 800 °C, presents a half hollow ball with porous structure (Fig. 2 c). At high magnification (Fig. 2 d) the surface of P800 is more rough than P400 and C800, which implies it can offer more sites for functionalization. As shown in Fig. 2 e, comparison sample C800, which directly carbonized at 800 °C without phosphoric acid impregnation, the carbon sphere morphology is preserved basically, only surface cracks and a small amount of pores (Fig. 2 f) are formed during the carbonization. With increasing the carbonization temperature from 400 to 800 °C, the surface morphology of the carbon sphere is changing from smooth to more porous because of enhancing the reaction between the phosphoric acid and BM-DVB precursor.

3.2 Raman spectra analysis

Raman spectroscopy can reflect the defect density of microcrystalline structure and the degree of graphitization of carbon material. First order Raman spectra for all carbon materials are shown in Fig. 3. Two distinct peaks can be observed around 1354-1369 cm^{-1} and 1589-1604 cm^{-1}, which correspond to D band and G band, respectively. The D band can be assigned to lattice defect in the structure, while G band reflecting the in-plane stretching vibration of sp^2 hybridized C=C bond. The position of D band decreases from 1369 cm^{-1} to 1354 cm^{-1} as carbonisation temperature increases from 400 to 700 °C and remains unchanged for all other carbons. The trend may be ascribed to disappearing sp^3-bonded amorphous structures with increasing carbonisation temperature [34]. The G band for P,N,O-doped carbons appear at 1604 cm^{-1} while for P-free carbon C800 at 1589 cm^{-1}. The difference could be attributed to compressive strain in graphite-like structure [34] due to the presence of phosphates/polyphosphates (see section 3.4). The area ratio of D band and G band (I_D/I_G) has been well recognized as an important parameter to evaluate the structure of carbons [35]. For carbon materials with relatively small graphene-like domains increasing the value of I_D/I_G is interpreted as increasing the ordering of aromatic clusters towards graphene-like networks with coherent domain sizes [34]. As the temperature increases the I_D/I_G values of phosphoric acid treated carbons increases from 1.5 to 4.5 which is accompanied by increasing aromatic cluster size from 1.6 to 2.9 nm (Fig. 3). The I_D/I_G ratio and aromatic cluster size for carbon C800 is close to that for carbon obtained by phosphoric acid activation at lower temperatures of 700 °C, suggesting that activating action of phosphoric acid creates more ordered carbon structure.

carbon	I_D/I_G	La/nm
P400	1.51	1.66
P500	1.44	1.62
P600	1.59	1.70
P700	2.14	1.97
P800	3.34	2.47
P900	3.42	2.49
P1000	4.46	2.85
C800	2.17	1.99

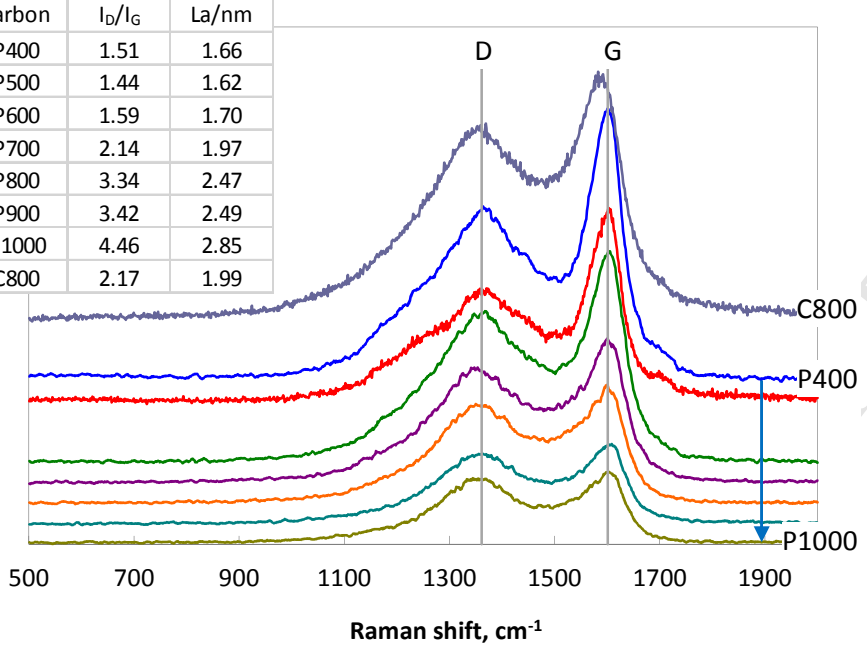

Fig. 3. Raman spectra of samples

3.3 Porous structure analysis

It is well known that the well-developed pore structure of the electrode materials is in favour of the contact with the electrolyte ions and increase the available specific surface area of carbon materials. Therefore, porous structure of resulted carbons was studied. Fig. 4 a shows nitrogen adsorption isotherms for selected carbons (for clarity reason, the isotherms of P700, P900 and P1000 that overlapped were not presented here). The nitrogen adsorption amount for P400 is quite small, indicating the phosphoric acid activation at low temperature (400 °C) is not sufficient to create porous structure in polymer-based carbon. With increasing heat treatment temperature from 500 to 600 °C, the N_2 sorption isotherms raises significantly and exhibits types IV with H4 hysteresis loop as classified by the IUPAC [36], which corresponds to the adsorption in slit-shaped micropores having a distribution of sizes and capillary condensation in mesopores. The sample P600 shows the highest nitrogen adsorption, which means the largest amount of micropores that contributes to the highest BET surface area. Further increasing carbonization temperature to 800 °C slightly decreased the nitrogen adsorption. The nitrogen uptake by C800 is significant at high relative pressures, which is characteristic of large mesopores in the carbon structure. Nitrogen adsorption isotherm for C800 carbon belongs to type IV with H1 hysteresis loop associated with pore blocking and wide pore size distribution [36]. Such results fit well with the morphology characterization which observed by the SEM.

The pore-size distributions (PSD) is a dominant factor that affect the electrode kinetics [37]. Herein, the PSD of the carbons which calculated by NLDFT method using slit pore model [38] are depicted in Fig.4 b. It can be clearly seen that the PSD of P400 is inconspicuous due to absence of pores, whereas the PSD for the samples derived at higher temperatures (500-1000 °C) show quite developed porosity, with an intense peak at 1.3 nm and 3.4 nm. Among them, P600 shows the highest peak at 1.3 nm, suggesting most of the micropores distributed in this size, which coincide with the

highest nitrogen adsorption amount of P600. On the contrary, the pore structure of C800 is mainly developed in the range of 10-24 nm pore sizes with maxima at 11 nm and 18 nm, which belong to mesopores. PSD of carbon C800 obtained without phosphoric acid retained the porous structure of parent copolymer [29, 30]. On the contrary, PSD for carbons obtained with phosphoric acid shows more developed microporous structure without large mesopores in the range 10-24 nm. These phenomena may be explained by redistribution of carbon material due to attack of phosphoric acid by the cleaving weak connecting bridges in polymer molecules at sub-pyrolysis temperatures. Subsequently, phosphoric acid catalyses the alkylation of aromatic structures or oligomerization of alkenes [39]. Thus, the attack of phosphoric acid leads to rearrangement of polymer material and thus disappearing the porosity initially present in the polymer precursor.

The porous structure parameters of all carbons (Table 1) show that micropores occupies a large fraction of total pore volume (55-60%) in carbons treated with phosphoric acid at 500–1000 °C, which allows classifying the carbons as micro/mesoporous. Such special porous structure is expected to be beneficial for the electrode performance in SCs: micropores are in favour of large amount of charge storage, while mesopores can provide fast ion diffusion path to the micropores of the carbons. With increasing the activation temperature from 400 to 600 °C, both S_{BET} and $V_{Total\ pore}$ are increased dramatically and reaches the highest values of 890 $m^2\ g^{-1}$ and 0.45$cm^3\ g^{-1}$ at 600 °C, respectively (Table 1). Heat treatment at higher temperatures of 700 °C results in decreasing porosity that may be attributed to contraction of carbon material [30]. Slight increase in S_{BET} and $V_{Total\ pore}$ for carbon P900 as compared to P800 could be ascribed to emptying of space occupied by polyphosphates due to thermal decomposition and reduction of phosphates to elemental phosphorus [40]. However, further increasing the activation temperature to 1000 °C leads to slight decreasing S_{BET} and $V_{Total\ pore}$ due to progressive contraction of carbon material. It is interesting to note that carbon C800 retains a mesoporous structure (V_{micro}/V_{total}=25%) due to lack of activating agent.

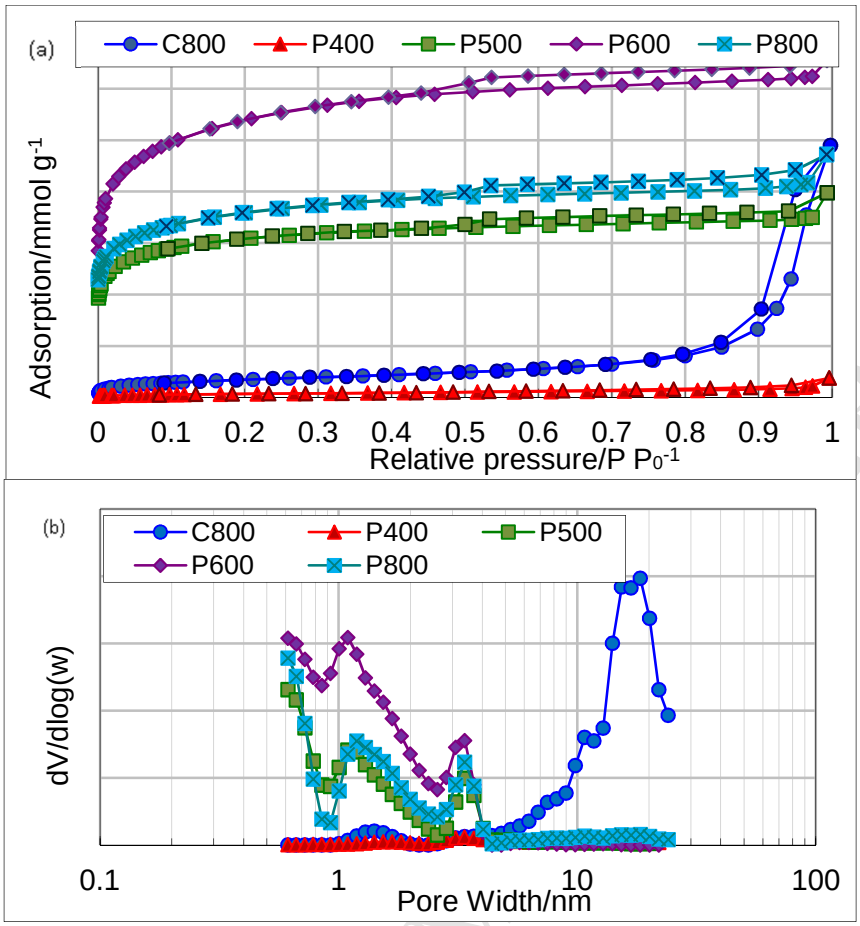

Fig. 4. (a) N_2 sorption isotherm and (b) Pore size distributions

Table 1. Porous structure parameters, oxygen, nitrogen and phosphorus contents, and specific capacitances of all carbon samples

Sample	S_{BET}/m^2 g^{-1}	$V_{total\ pore}$/cm^3 g^{-1}	V_{micro}/V_{total}/ %	Pore size/nm	Capacitance at 1.0 V and 0.1 A g^{-1}/F g^{-1}	Capacitance at 1.5 V and 0.1 A g^{-1}/F g^{-1}
C800	220	0.19	25	11, 18	5	--
P400	12	0.03	-	-	21	--
P500	520	0.28	57	1.3, 3.3	97	99
P600	890	0.45	56	1.2, 3.2	107	122
P700	675	0.35	60	1.3, 3.3	114	136
P800	595	0.33	55	1.3, 3.3	132	152

P900	650	0.35	60	1.2, 3.2	129	145
P1000	600	0.33	55	1.4, 3.3	91	114

3.4 Surface chemistry analysis

To verify the elemental composition of the carbons, both elemental analysis (EA) and X-ray photoelectron spectroscopy (XPS) were used to characterize the samples. As shown in Table 2, there are some distinctions between two measurements because EA is obtained for the elements in the bulk of carbons while XPS analysis is only tests 10-12 nm depth of the carbon surface/ matrix [41]. As can be seen from the EA results, all the carbon materials contain nitrogen. With the activation temperature increasing up to 800 °C (Table 2), the content of both bulk and surface nitrogen increases, whereas further increase of activation temperature leads to the decreasing of nitrogen concentration. The variation of nitrogen content occurs in paralel with surface concentration of phosphorus. This fact could be ascribed to the strong interaction of phosphric acid with nitrogen-containing polyimide polymer. Furthermore, it is clear that the amount of phosphorus and nitrogen measured by XPS reached the maxima of 11.17 at% and 2.79 at% in P800, respectively, corresponding to the tendency of phosphorus content in styrene-divinylbenzene based carbon (DB) as previously reported [42, 43], meanwhile the phosphorus content of P800 is 2 times higher than in DB. This result could be attributed to the more strong interaction of phosphric acid with nitrogen-containing polyimide polymer [42, 43].

Table 2 Carbon, nitrogen and hydrogen bulk content in the carbon samples obtained from elemental analysis (EA) and surface concentration of oxygen, nitrogen and phosphorus derived from XPS

Sample	EA bulk content/wt%			XPS surface concentration/at%			
	C	N	H	C	O	N	P
P400	59.95	2.79	3.64	86.47	10.76	2.08	0.69
P500	63.89	2.94	3.46	82.90	13.39	2.07	1.64
P600	56.22	3.22	4.51	78.77	11.14	2.13	4.60
P700	57.66	3.62	3.40	74.81	11.29	2.22	8.07
P800	56.02	3.74	3.69	74.75	11.77	2.79	11.17
P900	58.08	2.91	3.27	76.17	12.34	2.55	8.94
P1000	64.49	1.98	3.46	81.89	11.00	1.66	5.45
C800	60.45	2.52	3.23	85.68	12.89	2.02	-

Table 3. The distributions of oxygen, phosphorous and nitrogen functional groups obtained from the deconvolution of O1s, P2p and N1s XPS peaks.

Element	BE/eV	Assignment	Content/Area/%							
			P400	P500	P600	P700	P800	P900	P1000	C800
O	531.2	C=O, P=O	6.00	32.60	36.15	35.44	35.36	34.17	25.95	5.28
	532.2	C−O−C, C−OH	22.75	42.30	39.12	50.45	26.04	32.36	35.16	28.03
	533.5	P−O−P,−COOH	34.94	-	19.64	11.00	30.79	23.52	34.50	29.71
	534.5	Chemisorbed O/H_2O	36.31	25.10	5.09	3.11	7.81	9.95	4.39	36.98
	Total	Content/at%	10.76	13.39	11.14	11.29	11.77	12.34	11.00	12.89
P	132.2	Phosphates	-	44.32	15.31	4.64	-	-	-	-
	133.1	Pyrophosphates	-	40.49	46.22	50.16	57.64	48.82	45.59	-
	134.2	Metaphosphates	-	15.19	38.47	37.28	36.12	43.09	46.81	-
	136.0	P_4O_{10}	-		-	7.92	6.24	8.09	7.60	-
	Total	Content, at%	0.69	1.64	4.60	8.07	11.17	8.94	5.45	-
N	398.1	Pyridinic N	10.47	32.30	35.90	21.63	23.60	21.72	33.72	20.58
	399.6	Pyrrolic-like N	30.50	30.81	31.16	36.24	37.07	39.18	22.68	37.08
	401.0	Graphitic N	43.62	25.80	27.72	33.46	33.61	31.50	24.01	30.60
	403.0	Pyridinic N-oxide	15.41	11.09	5.22	8.67	5.72	7.60	19.59	11.74
	Total	Content/at%	2.08	2.07	2.13	2.22	2.79	2.55	1.66	2.02

As shown in Table 3, the deconvolution of the high-resolution P2p core level signals of carbons reveals three to four components at binding energies (BE) around 132, 133, 134 and 136 eV which were assigned to phosphates $[PO_4]^{3-}$ (P-I, 132.2 eV) [44], pyrophosphates $[P_2O_7]^{4-}$ (P-II, 133.1 eV) [41], metaphosphates $[PO_3]^-$ (P-III, 134.2 eV) [45], and phosphorus pentoxide P_4O_{10} (P-IV, 136.0 eV) [46], respectively.

High-resolution O1s core level signals of carbons were deconvoluted to the binding energies of oxygen functionalities around 531.2 eV, 532.2 eV, 533.5 eV and 534.5 eV and were assigned to the C=O quinone type groups and P=O groups (O-I) [47], C−O−C ether groups and/or phenol C−OH groups (O-II) [41], P−O−P pyrophosphate groups and/or COOH carboxylic groups (O-III) [46] and chemisorbed oxygen and water (O-IV) [48], respectively.

Deconvoluted nitrogen functionalities were assigned to pyridinic nitrogen (N-6, BE=398 eV), pyrrolic-like nitrogen (N-5, BE=399.5 eV), graphitic nitrogen (N-Q, BE=401 eV), and pyridine-N-oxides (N-X, BE=403 eV), respectively [49, 50]. The pyridinic nitrogen (N-6) is present in a six-membered ring at the edge of the carbon, bonding with carbon atoms in hybridization way,

contributing only one *p* electron to the aromatic π-orbital system of carbon atoms, thus has the lowest binding energies. Whereas pyrrolic-like nitrogen (N-5) occurring in five-membered ring and pyridone nitrogen which bond a six-membered rings with oxygen [51] contribute two *p* electrons to the π -orbital of carbon atoms, thus binding energies are higher. The graphitic nitrogen (N-Q) substitutes carbon atom in multi-six-membered rings, therefore the N-Q is distributed within the carbon matrix, whereas the N-6 and N-5 are mainly found at the edge of the carbon. It was also reported [52] that in the vicinity of N-5, carbon atoms are much more positively charged than near the N-6, which may benefit to the capacitive behaviour of the carbons in aqueous electrolyte.

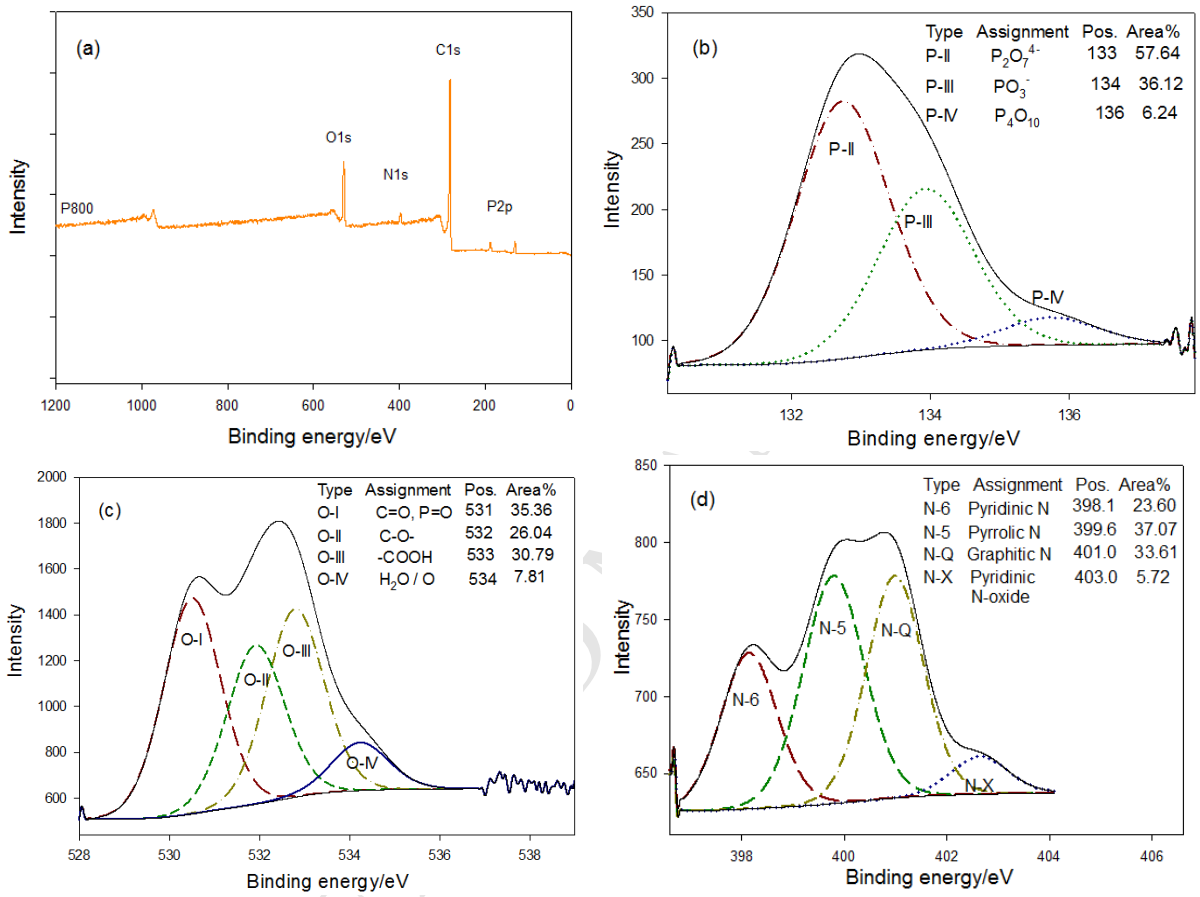

Fig.5. (a) XPS survey spectrum of P800; (b-d) Deconvolution analyses of high resolution XPS spectra of P2p, O1s and N1s for P800.

The phosphorus, oxygen and nitrogen are combined with each other in different structures in the carbons, such as non-bridging oxygen (O-I) bonded to phosphorus in the form of P=O, bridging oxygen (O-II) contribute the carbon-oxygen single bond with phosphorus like C-O-P, the phosphorus bonded to nitrogen in P-N and P=N [53].

It can be seen that carbon P800 contains the largest amount of phosphorous and nitrogen, so we take it as an example; the XPS spectra, deconvolution analysis of P2p, O1s and N1s core level peaks of P800 are displayed in Fig.5. It is clear that only P800 has three types of phosphorus functional groups, that are pyrophosphates (P-II), metaphosphates (P-III), and phosphorus pentoxide P_4O_{10} (P-IV), among them, P-II is the major component. Nevertheless, phosphate $[PO_4]^{3-}$ (P-I) is the main

component in P500, while with further increasing the activation temperature, P-I disappears and P-IV appears in the carbon structure and reach the highest value in P900 because P-I is easy to decompose at high temperature. In addition to the presence of P-IV, the chemically adsorbed water and oxygen content is relatively high in P900 which could be attributed to the desiccant effect of P_4O_{10} [8]. The double bonded oxygen C=O, P=O (O-I) is the main component in carbon P800, while the nitrogen functional groups are mainly in N-5 and N-Q. The single bonded oxygen C−O− (O-II) is the second most abundant form that may take part in some redox reactions.

As can be seen from Table 3, the amounts of surface phosphorus of P400 is too low (0.69 at%) to deconvolute the high-resolution P2p core level peaks. This is caused by low activation temperature insufficient for introduction of phosphorus and developing porous structure. Whereas the phosphorus content in the samples obtained at higher temperatures (500-1000 °C) is much higher due to the enhanced reactivity of phosphoric acid at high temperature to the polyimide precursor. As a result, carbons obtained at high temperature show high phosphorus content and well-developed porous structure.

These results clearly indicate that activation temperature can greatly influence the type of surface chemistry in addition to the various porous structures, and therefore, those two factors are expected to affect the electrochemical performance of carbons in different ways.

3.5 Electrochemical performances of the carbon

3.5.1 Electrochemical impedance test

Electrochemical impedance spectroscopy (EIS) study was performed within the frequency domain of 0.01-10^5 Hz to investigate electrochemical systems involving P,N,O-co-doped carbons. Nyquist plot (Fig. 6a,b) for all carbons presents a depressed semicircle in middle and high frequency region. The intersection of curve with real impedance axis represents the equivalent series resistance (ESR). With increasing carbonization temperature ESR decreases reaching minimum value for carbon obtained at 800 °C and increases at higher temperatures (Fig 6b, Table 4). The highest ESR value is for P-free carbon C800. The radius of semi-circle in the medium-high frequency domain represents the charge transfer resistance (CTR), which decreases with carbonization temperature up to 800 °C and increases at higher temperatures. The highest CTR is observed for carbon C800 obtained without addition of phosphoric acid. The temperature dependence of phosphorus, oxygen and nitrogen content (Table 2) correlate well with reciprocal of ESR, suggesting crucial role of heteroatom species for supercapacitor performance by facilitating the formation of EDL through the enhanced wettability [54] and proton transfer [55].

In the low frequency domain Nyquist plot typically comprises linear part which usually deviates from both the Warburg impedance line and the vertical line of purely capacitive behaviour [56]. The non-ideal behaviour at low frequencies originates from frequency dispersion caused by limited diffusion, slow adsorption of anions and distribution of pore sizes and shapes. With increasing carbonization temperature, the slope of a line in low frequency domain increases and tends to approach almost vertical line, suggesting capacitive behaviour (Fig. 6a). The most gently sloping and upwardly concave curve is observed for carbon C800 obtained without phosphoric acid, indicating strongly inhomogeneous charge-discharge process. The differences between Nyquist plots of phosphorus-containing carbons and P-free sample C800 suggests impact of phosphorus, oxygen and nitrogen species on capacitive behaviour of carbon.

Positive values of imaginary component of the impedance in high frequency domain (Fig. 6b) is connected with protons (1 mol L^{-1} H_2SO_4) fast reacting to the electric field oscillations in the samples [57].

Bode plot of frequency dependence of phase angle (Fig. 6c) shows that with increasing carbonization temperature the phase angle at low frequencies increases and reaches the value -90° characteristic to purely capacitive performance. The phase angle for P-free carbon C800 is only -62° that is far from ideal capacitive behaviour.

Fig. 6d shows frequency dependence of imaginary part of the capacitance [58, 59]. The maximum of the curve is a characteristic of the electrode system and can be ascribed to a transition point from purely resistive to purely capacitive behaviour [58]. The frequency where this maximum occurs increases with increasing carbonization temperature reaching a maximum for carbon P800 (Fig. 6d, Table 4). The inverse of the characteristic frequency is a time constant that is a quantitative measure of how fast the device can be charged and discharged reversibly. Time constant decreases from 19 s to 0.7 s as carbonization temperature increases up to 800 °C (Table 4). The longest time constant is for P-free carbon C800. This suggests crucial role of phosphorus, oxygen and nitrogen heteroatoms for facilitating supercapacitor performance.

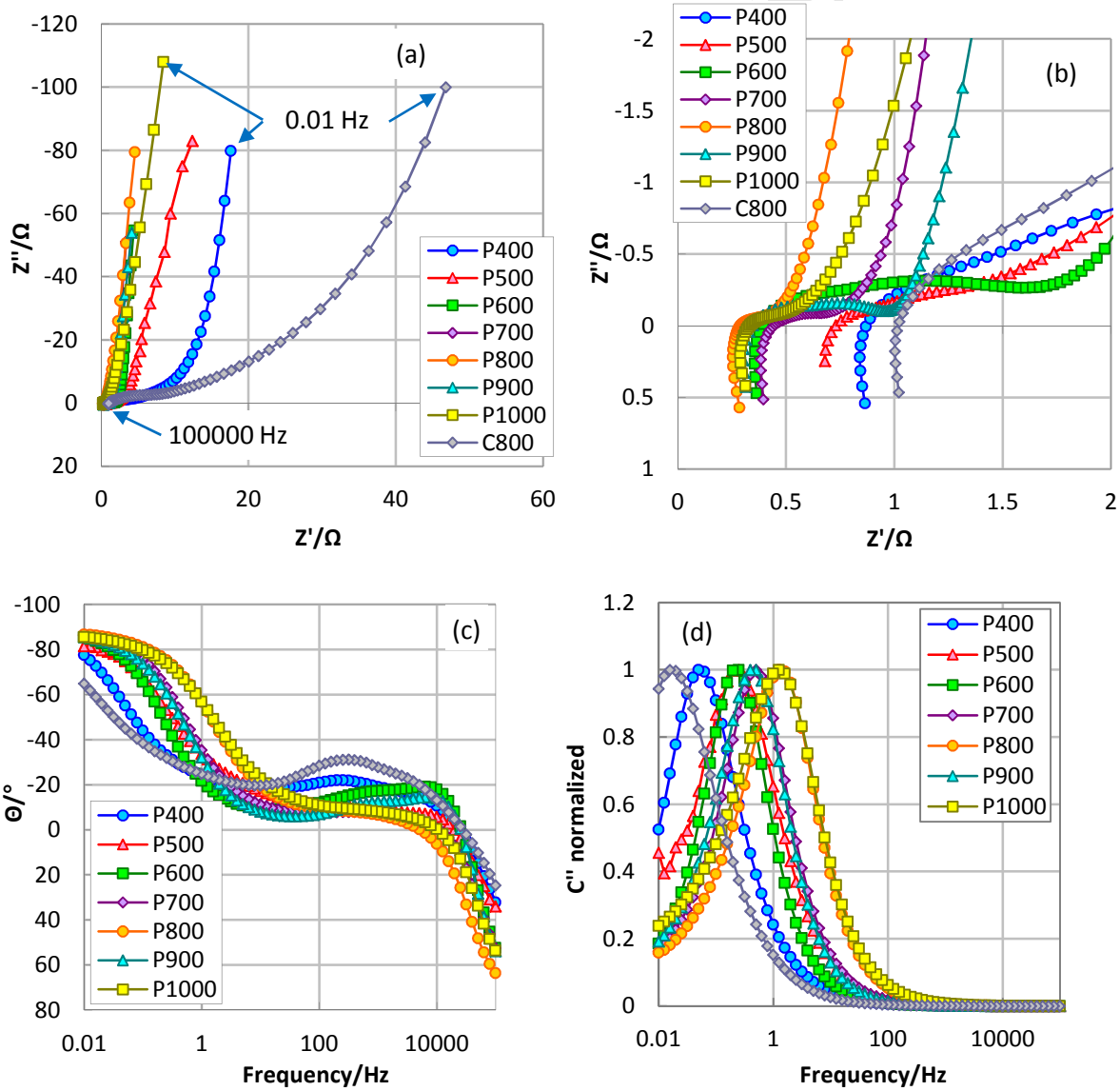

Fig. 6. (a) Original Nyquist plot; (b) Amplified high frequency part of Nyquist plot of all samples; (c) Bode plot of frequency dependence of phase angle; (d) variation of C'' (imaginary) with frequency.

Table 4. Electrochemical characteristics of P,N,O-doped carbons obtained from EIS.

Carbon	Equivalent series resistance/Ω	Frequency for C'' max/Hz	Time constant/s
P400	0.87	0.05	18.6
P500	0.73	0.22	4.5
P600	0.39	0.22	4.5
P700	0.44	0.50	2.0
P800	0.29	1.35	0.7
P900	0.34	0.44	2.3
P1000	0.33	1.28	0.8
C800	1.02	0.02	58.4

3.5.2 Cyclic voltammetry test

The electrochemical performances of the samples were first evaluated by cyclic voltammetry techniques by using three-electrode cells (3E) in 1 mol L^{-1} H_2SO_4 aqueous electrolyte. Fig.7 shows the CV curves obtained at the scan rate of 100 mV s^{-1} in the range 0-1.0 V. The response currents of P400, P500 and C800 are very low, demonstrating the low capacitances, which can be attributed to the insufficiently developed porous structure, absence of lattice defect and less active sites of the carbons. Such results are also in line with analysis of porous structure and Raman spectra (Fig. 3). P600 has the highest surface area and the highest volume of micropores (Fig. 4, Table 1), however, its CV profile shows some distortion, which is caused by the low electrical conductivity due to relatively low activation temperature as shown in the electrochemical impedance test (Fig. 6, Table 4). As for the other four samples (P700, P800, P900, P1000), the basically rectangular shapes of CV curves characteristic to electric double layer capacitor (EDLC) imply that the dominant charge-storage mechanism is accumulation of ionic charges in the double-layer between the electrode and the electrolyte. These carbons show the superior capacitance behaviour and good reversibility; moreover, a few pairs of humps are observed at 0.4 - 0.6 V vs. Ag/AgCl/3M KCl in the CV profiles typically related to the pseudocapacitance contributed from the surface oxygen and nitrogen functionalities, which can be attributed to the high content of C=O quinone type groups and pyrrolic-like N revealed by XPS (Table 3) in these samples. By contrast, we found that the surface areas of P800, P500 and P1000 are similar (Table 1, the differences less than 80 m^2 g^{-1}), but the response current of P800

shows the highest value, indicating the largest capacitance value. The difference between CV curves of these three samples provides reason enough to conclude that the surface area is not the determining factor for the capacitive performance. The capacitance of carbon electrode also depends on the surface chemistry, the morphology and the degree of lattice defects.

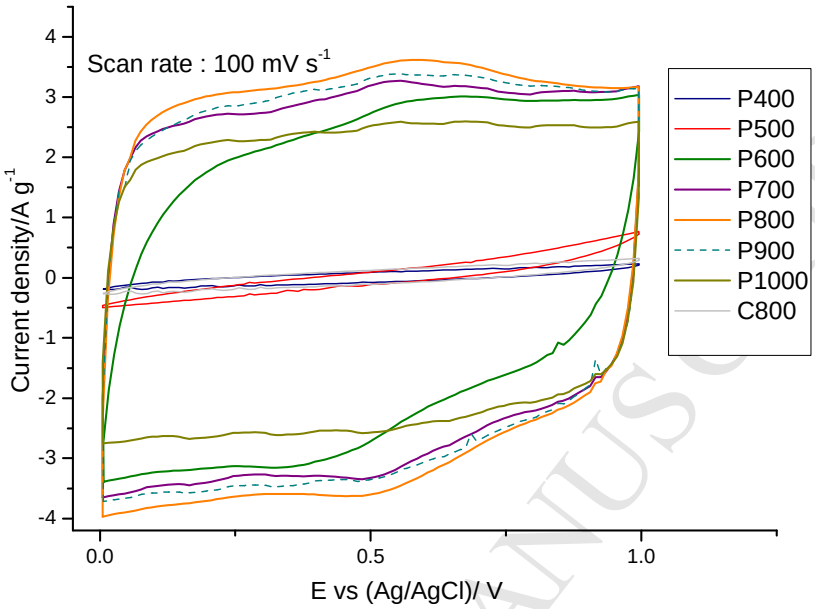

Fig. 7. CV curves of samples at 100 mV s^{-1} obtained in 3E configuration

3.5.3 Galvanostatic charge/discharge test

Further to evaluate the electrochemical performance of all samples as supercapacitor electrodes as well as to reveal the role of phosphorus, nitrogen and oxygen functionalities, galvanostatic charge/discharge (GC) measurements were carried out in two-electrode cells (2E) at different current densities. Fig. 8 shows GC curves measured at the current density of 1 A g^{-1} and 0.05 A g^{-1}. It is not surprised that the charge-discharge times of P400 and C800 carbons are very short; the symmetry of the GC curves for these two samples is poor. Moreover, there appears a large IR drop in the discharge GC curves of P500, suggesting the high equivalent series resistance and dissatisfied capacitance performances of these three samples. The potential of the other samples changed linearly with time, thus their GC curves show the nearly symmetric triangular shape and low IR drop even at high current density of 1 A g^{-1} (Fig. 8), demonstrating typical capacitive performance and high efficiency during the charge-discharge process. As show in Fig. 8a, the charge-discharge time of P600 and P800 are quite close to each other, suggesting the similar capacity at 0.05 A g^{-1} current load. When the current density increased to 1 A g^{-1} (Fig. 8 b), the charge-discharge time of P600 becomes much shorter than P800 and IR drop can be found obviously in GC curve for P600, indicating the poorer capacitive performance. It can be explained by the following two aspects. One is the low electrical conductivity of P600. The other reason can be linked to less amount of electrophilic functional groups in carbon P600. P800, however, due to the synergetic effect of phosphorous, nitrogen and oxygen functional groups, has a good electrochemical stability and reversibility even at high current density of 1 A g^{-1}. In addition, P1000 exhibits the perfect symmetric triangular-shaped GC curves that are typical for

electric double layer capacitors. Such results are related well with the electrochemical impedance and cyclic voltammetry (CV) measurement.

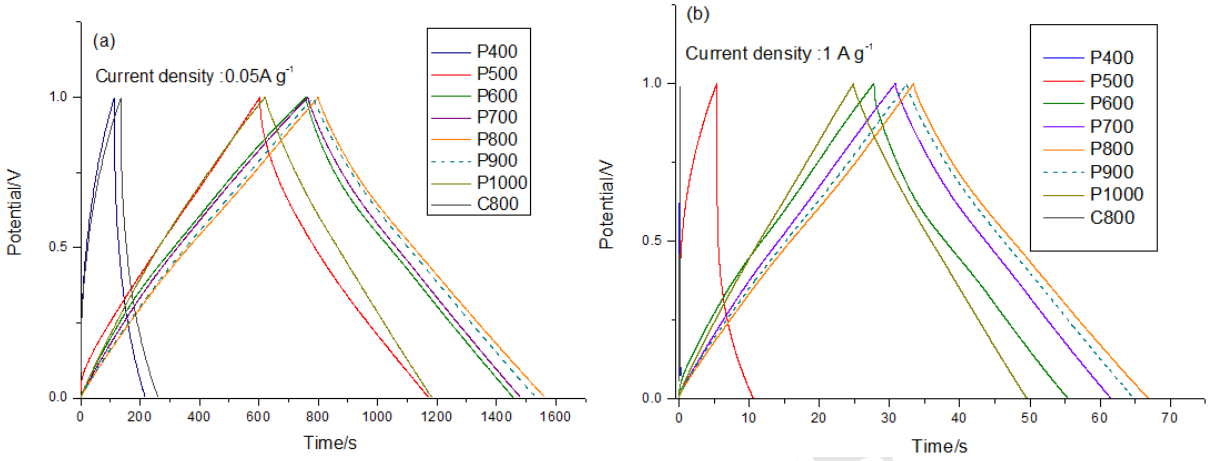

Fig.8. Galvanostatic charge/discharge profiles of samples measured in 2E at the current density of (a) 0.05 A g^{-1} and (b) 1 A g^{-1}

The dependence of capacitance on current density is depicted in Fig.9. As the current density increases to 1 A g^{-1}, C_{single} of all samples tend to decrease. This fact can be ascribed to the spatial hindrance; electrolyte ions only can diffuse into part of the pores of carbon material at fast charge/discharge rates. It is obviously seen that P800 provides the highest capacitance of 157 F g^{-1} at 0.05 A g^{-1}, as the current density increasing to 1 A g^{-1}, the capacitance retention ratio is as high as 87%, while the capacitance of C800 is only 20 F g^{-1} at 0.05 A g^{-1}. Furthermore, P800 and P1000 show the similar porous structures (Table 1) but the capacitance differs a lot (157 F g^{-1} vs. 112 F g^{-1}) at the current density of 0.05 A g^{-1}. By comparison with the Raman, EA, and XPS results, it can be found that the I_D/I_G ratio of P800 is higher than for P1000, indicating the more defects in P800; and P800 contains more pyrophosphates, graphitic N, pyrrolic N and C=O than P1000, which improved the electrochemical stability, electrical conductivity and pseudocapacitance of P800.

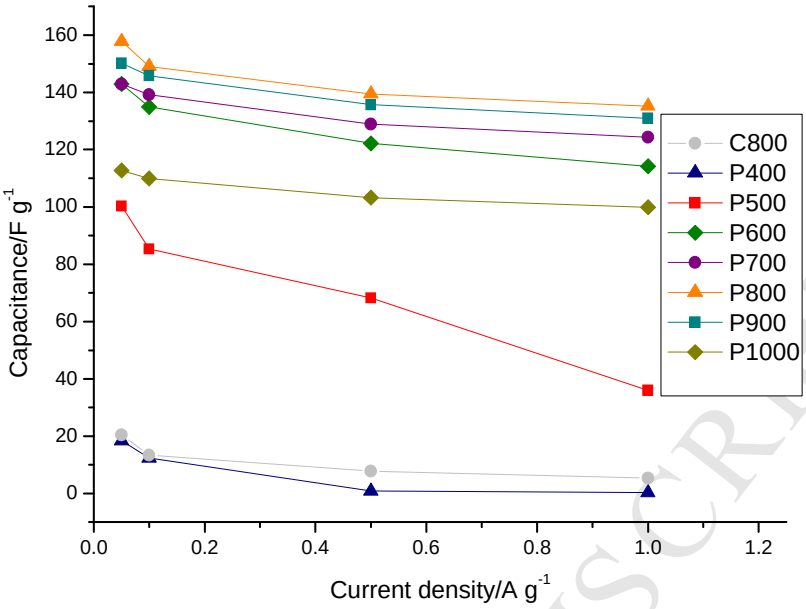

Fig. 9. Specific capacitance decay of all carbons as a function of current density

3.5.4 Wide potential window test

As shown in the equation (3) the energy density is proportional to the square of operating potential (V). Therefore, increasing the operating potential can greatly enhance the energy density. To investigate the possibility of utilizing co-doped polymer-based carbons (P500-P1000) in an aqueous electrolyte beyond the decomposition potential of water (1.23 V), a wide potential window tests were conducted in 2E setup by stepwise increasing the potential range from 0-1.0 V to 0-1.5 V in 1 mol L^{-1} H_2SO_4 electrolyte by using GC test. Table 1 lists the C_{single} at the current density of 0.1 A g^{-1} at different potential ranges which obtained according to Equation (1) by using the discharge branch. As can be seen, with the increase of potential window, the C_{single} of P800 increased obviously from 132 to 152 F g^{-1}. Taking into account the results of pore structure, Raman spectroscopy, and XPS analysis, the superior performance of P800 under high potential can be attributed to (i) the micropore-mesopore structure facilitates the fast transmission of electrolyte ions; (ii) the high defect density provides high density of active sites; (iii) abundance of phosphates facilitate the formation of EDL through the enhanced wettability [54] and proton transfer [55] by increasing ionic conductivity through Grotthuss mechanism [60]; (iv) abundance of surface functionality increases capacitance through fast Faradic reactions (pseudocapacitance); and (v) phosphate/polyphosphates blocks active sites of carbon material which could be oxidised under high current load [61].

Fig. 10 a and b show the GC curves of six samples at 0.1 A g^{-1} in the potential range of 0-1.4 V and 0-1.5 V, respectively. It can be seen that most of the GC curves are symmetric in Fig. 10 a, indicating the superior capacitive performance, whereas when the potential increased to 1.5 V (Fig. 10 b) a plateau appears at the vertex potential, which suggests the saturation of the carbon surface. Therefore, we can speculate that 1.5 V is the highest potential operating limit for this series of carbon-based supercapacitor in sulphuric acid electrolyte.

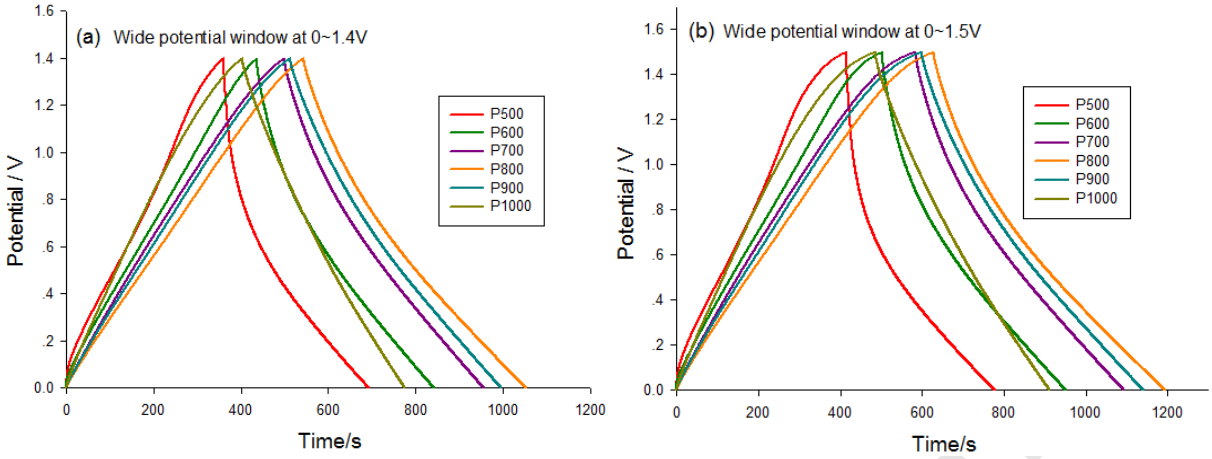

Fig. 10. GC curves of six samples at 0.1 A g^{-1} and the potential range of a) 0-1.4 V and b) 0-1.5 V

The energy density and power density at different potential ranges and current loads were calculated by equations 3 and 4 based on the galvanostatic test (Fig.11). It can be seen that the energy density of P800 at the operating potential of 1.5 V is 2.2 times higher than at 1.0 V for the same power density. When the power density of P800 increased to 750 W kg^{-1}, the energy density remains at 10 Wh kg^{-1} for 1.5 V, suggesting that much energy could be quickly delivered.

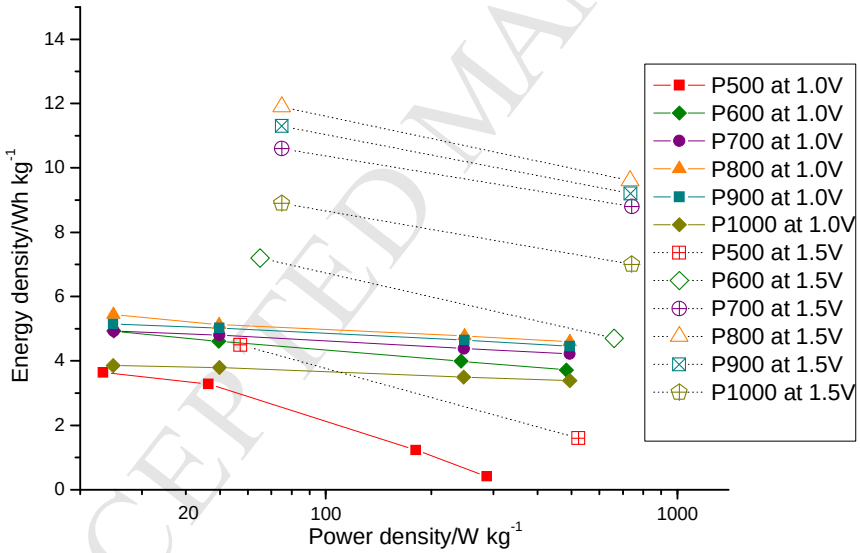

Fig. 11. Ragone plot of six samples measured in 2E at different potential window.

3.5.5 Cycling performance under the wide potential window

The cycling durability of the carbon is the key factor determining the life and stability of the supercapacitor. Galvanostatic charge-discharge test under 5 A g^{-1} and 0-1.5 V were employed to test the cycling stability of the six samples for 10000 cycles. As shown in Fig. 12, all samples show deterioration of the specific capacitance in different extent, among them, the attenuation of P500, P600 and P700 is more evident. Although the retention ratio of P1000 is high, its initial capacity is quite low with only 95 F g^{-1}. P800 with the highest initial capacity shows a stable performance with specific

capacitance retention of 85% (from 132 F g^{-1} to 112 F g^{-1}). It is speculated that this phenomenon is caused by the inhibition effect of P functionalities in P800 that can suppress the oxidation of carbon surface [61, 62], together with the well-developed micropore-mesopore structure that facilitates the fast transmission of electrolyte ions on the core-shell carbon sphere during the long cycling test and harsh condition.

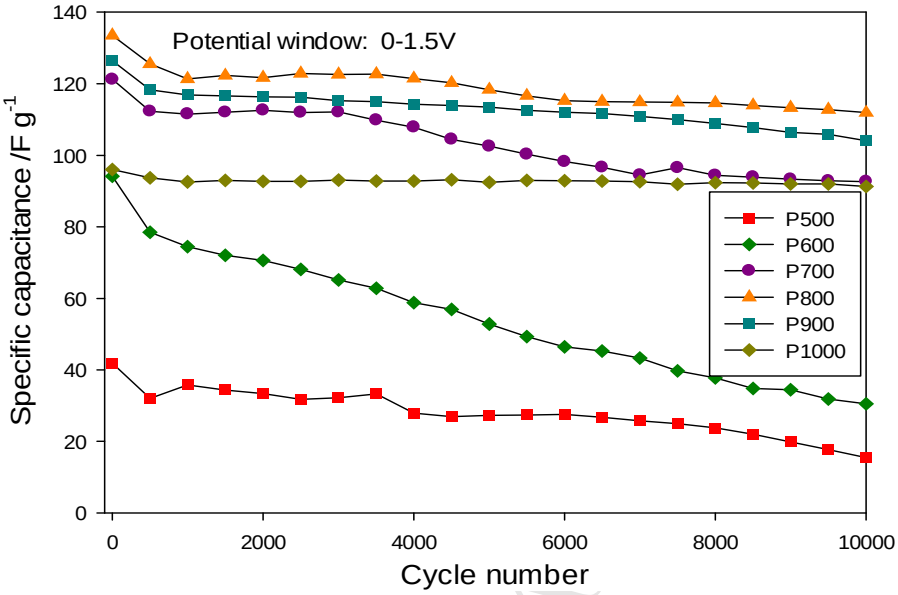

Fig.12. Cycling test of GC at 0-1.5 V and current density of 5 A g^{-1}

4. Conclusions

In conclusion, we have developed a series of phosphorus, nitrogen and oxygen co-doped polymer-based core-shell carbon electrode for SCs, in which the co-doped carbon materials were prepared by phosphoric acid activation of polyimide copolymer. The activation temperature was found to be very crucial in co-doping and structure formation processes. It was found that carbon obtained at 800 °C (P800) with a core-shell porous structure and a P, N and O doping level of 11.17 at%, 2.79 at% and 11.77 at% respectively, shows a capacitance of 157 F g^{-1} at the current density of 0.05 A g^{-1}. Moreover, the electrode can survive at a wide potential window of 1.5 V with only 15% decrease in capacity after 10000 cycles at a current density of 5 A g^{-1}, providing a high energy density of 10 Wh kg^{-1} and a high power density of 750 W kg^{-1}. The outstanding performance of P,N,O-doped carbons is attributed to (i) the micropore-mesopore structure facilitates the fast transmission of electrolyte ions; (ii) the increasing aromatic cluster size provides high electron conductivity; (iii) abundance of phosphates facilitate the formation of EDL through the enhanced wettability and proton transfer by increasing ionic conductivity through Grotthuss mechanism; (iv) abundance of surface functionality increases capacitance through fast Faradic reactions (pseudocapacitance); and (v) phosphates/polyphosphates block active sites of carbon material which could be oxidised under high current load. These results may shed some light on opening up strategies for designing nanostructured carbons, and on developing new heteroatoms doped carbon electrodes with good performance for SCs.

References

[1] F. Béguin, K. Szostak, G. Lota, E. Frackowiak, A Self-Supporting Electrode for Supercapacitors Prepared by One-Step Pyrolysis of Carbon Nanotube/Polyacrylonitrile Blends, Adv. Mater. 17 (2005) 2380.

[2] E. Raymundo-Piñero, F. Leroux, F. Béguin, A high-performance carbon for supercapacitors obtained by carbonization of a seaweed biopolymer, Adv. Mater. 18 (2006) 1877.

[3] Y. Wen, T.E. Rufford, D. Hulicova-Jurcakova, L. Wang, Nitrogen and Phosphorous Co-Doped Graphene Monolith for Supercapacitors, ChemSusChem 9 (2016) 513.

[4] G. Xu, B. Ding, J. Pan, J. Han, P. Nie, Y. Zhu, Q. Sheng, H. Dou, Porous nitrogen and phosphorus co-doped carbon nanofiber networks for high performance electrical double layer capacitors, J. Mater. Chem. A 3 (2015) 23268.

[5] D. Hulicova-Jurcakova, A.M. Puziy, O.I. Poddubnaya, F. Suárez-García, J.M.D. Tascón, G.Q. Lu, Highly stable performance of supercapacitors from phosphorus-enriched carbons., J. Am. Chem. Soc. 131 (2009) 5026.

[6] K. Fic, E. Frackowiak, F. Béguin, Unusual energy enhancement in carbon-based electrochemical capacitors, J. Mater. Chem. 22 (2012) 24213.

[7] X. Wu, L.R. Radovic, Inhibition of catalytic oxidation of carbon/carbon composites by phosphorus, Carbon 44 (2006) 141.

[8] C. Huang, A.M. Puziy, T. Sun, O.I. Poddubnaya, F. Suárez-García, J.M.D. Tascón, D. Hulicova-Jurcakova, Capacitive Behaviours of Phosphorus-Rich Carbons Derived from Lignocelluloses, Electrochim. Acta 137 (2014) 219.

[9] B. Li, F. Dai, Q. Xiao, L. Yang, J. Shen, C. Zhang, M. Cai, Nitrogen-doped activated carbon for a high energy hybrid supercapacitor, Energy Environ. Sci. 9 (2016) 102.

[10] Y. Wang, B. Fugetsu, Z. Wang, W. Gong, I. Sakata, S. Morimoto, Y. Hashimoto, M. Endo, M. Dresselhaus, M. Terrones, Nitrogen-doped porous carbon monoliths from polyacrylonitrile (PAN) and carbon nanotubes as electrodes for supercapacitors, Scientific Rep. 7 (2017) 40259.

[11] Z. Peng, R. Ye, J.A. Mann, D. Zakhidov, Y. Li, P.R. Smalley, J. Lin, J.M. Tour, Flexible Boron-Doped Laser-Induced Graphene Microsupercapacitors, Acs Nano 9 (2015) 5868.

[12] T.J. Bandosz, T. Z. Ren, Porous carbon modified with sulfur in energy related applications, Carbon 118 (2017) 561.

[13] Y. Li, G. Wang, T. Wei, Z. Fan, P. Yan, Nitrogen and sulfur co-doped porous carbon nanosheets derived from willow catkin for supercapacitors, Nano Energy 19 (2015) 165.

[14] T.X. Shang, R.Q. Ren, Y.M. Zhu, X.J. Jin, Oxygen- and nitrogen-co-doped activated carbon from waste particleboard for potential application in high-performance capacitance, Electrochim. Acta 163 (2015) 32.

[15]Y. Zhou, R. Ma, S.L. Candelaria, J. Wang, Q. Liu, E. Uchaker, P. Li, Y. Chen, G. Cao, Phosphorus/sulfur Co-doped porous carbon with enhanced specific capacitance for supercapacitor and improved catalytic activity for oxygen reduction reaction, J. Power Sources 314 (2016) 39.

[16] D. W. Wang, F. Li, M. Liu, G.Q. Lu, H.M. Cheng, 3D Aperiodic Hierarchical Porous Graphitic Carbon Material for High-Rate Electrochemical Capacitive Energy Storage, Angew. Chem. 120 (2008) 379.

[17] H. Jiang, P.S. Lee, C. Li, 3D carbon based nanostructures for advanced supercapacitors, Energy Environ. Sci. 6 (2012) 41.

[18] G. Zhang, Y. Song, H. Zhang, J. Xu, H. Duan, J. Liu, Radially Aligned Porous Carbon Nanotube Arrays on Carbon Fibers: A Hierarchical 3D Carbon Nanostructure for High-Performance Capacitive Energy Storage, Adv. Funct. Mater. 26 (2016) 3012.

[19] C. Wang, F. Li, H. Qu, Y. Wang, X. Yi, Y. Qiu, Z. Zou, Y. Luo, B. Yu, Fabrication of three dimensional carbon nanotube foam by direct conversion carbon dioxide and its application in supercapacitor, Electrochim. Acta 158 (2015) 35.

[20] F. Barzegar, A. Bello, O.O. Fashedemi, J.K. Dangbegnon, D.Y. Momodu, F. Taghizadeh, N. Manyala, Synthesis of 3D porous carbon based on cheap polymers and graphene foam for high-performance electrochemical capacitors, Electrochim. Acta 180 (2015) 442.

[21] A. Bello, F. Barzegar, D. Momodu, J. Dangbegnon, F. Taghizadeh, N. Manyala, Symmetric supercapacitors based on porous 3D interconnected carbon framework, Electrochim. Acta 151 (2015) 386.

[22] M. Ree, High performance polyimides for applications in microelectronics and flat panel displays, Macromol. Res. 14 (2006) 1.

[23] I.F. Davydova, N.S. Kavun, Glass plastics in aviation and rocket engineering, Glass Ceram. 69 (2012) 134.

[24] E.R. Rangel, E.M. Maya, F. Sánchez, J.G.D.L. Campa, M. Iglesias, Palladium-heterogenized porous polyimide materials as effective and recyclable catalysts for reactions in water, Green Chem. 17 (2014) 466.

[25] B.S. Ghanem, R. Swaidan, E. Litwiller, I. Pinnau, Ultra-microporous triptycene-based polyimide membranes for high-performance gas separation, Adv. Mater. 26 (2014) 3775.

[26] M. Inagaki, T. Takeichi, Y. Hishiyama, A. Oberlin, High quality graphite films produced from aromatic polyimides, Chem. Phys. Carbon 26 (1999) 245.

[27] A.M. Puziy, O.I. Poddubnaya, B. Gawdzik, M. Sobiesiak, M.M. Tsyba, Phosphoric acid activation-Functionalization and porosity modification, Appl. Surf. Sci. 253 (2007) 5736.

[28] M. Sobiesiak, B. Gawdzik, Thermal properties of porous copolymers of BM-DVB and their carbonization products, New Carbon Mater. 26 (2011) 137.

[29] A.M. Puziy, O.I. Poddubnaya, M. Sobiesiak, B. Gawdzik, Structural and surface heterogeneity of phosphorus-containing polyimide-derived carbons: effect of heat treatment temperature, Adsorption (2013) 717.

[30] A.M. Puziy, O.I. Poddubnaya, M. Sobiesiak, B. Gawdzik, Assessment of the structural evolution of polyimide-derived carbons obtained by phosphoric acid activation using Fourier transform infrared and Raman spectroscopy, Adsorpt. Sci. Technol. 35 (2017) 403.

[31] A. Sadezky, H. Muckenhuber, H. Grothe, R. Niessner, U. Pöschl, Raman microspectroscopy of soot and related carbonaceous materials: Spectral analysis and structural information, Carbon 43 (2005) 1731.

[32] A.C. Ferrari, J. Robertson, Interpretation of Raman spectra of disordered and amorphous carbon, Phys. Rev. B. 61 (2000) 14095.

[33] J.P. Olivier, Modeling physical adsorption on porous and nonporous solids using density functional theory, J. Porous Mater. 2 (1995) 9.

[34] J. McDonald-Wharry, M. Manley-Harris, K. Pickering, Carbonisation of biomass-derived chars and the thermal reduction of a graphene oxide sample studied using Raman spectroscopy, Carbon 59 (2013) 383.

[35] M.S. Dresselhaus, A. Jorio, R. Saito, Characterizing Graphene, Graphite, and Carbon Nanotubes by Raman Spectroscopy, Annu. Rev. Condens. Matter Phys. 1 (2010) 89.

[36] M. Thommes, K. Kaneko, A. V. Neimark, J.P. Olivier, F. Rodriguez-Reinoso, J. Rouquerol, K.S.W. Sing, Physisorption of gases, with special reference to the evaluation of surface area and pore size distribution (IUPAC Technical Report), Pure Appl. Chem. 87 (2015) 1051.

[37] G. Gryglewicz, J. Machnikowski, E. Lorenc-Grabowska, G. Lota, E. Frackowiak, Effect of pore size distribution of coal-based activated carbons on double layer capacitance, Electrochim. Acta 50 (2005) 1197.

[38] A.M. Puziy, O.I. Poddubnaya, B. Gawdzik, M. Sobiesiak, Comparison of heterogeneous pore models QSDFT and 2D-NLDFT and computer programs ASiQwin and SAIEUS for calculation of pore size distribution, Adsorption 22 (2016) 459.

[39] M. Jagtoyen, F. Derbyshire, Activated carbons from yellow poplar and white oak by H_3PO_4 activation, Carbon 36 (1998) 1085.

[40] A.M. Puziy, J.M.D. Tascón, Ch. 8, Adsorption by Phosphorus-Containing Carbons, 2012.

[41] A.M. Puziy, O.I. Poddubnaya, R.P. Socha, J. Gurgul, M. Wisniewski, XPS and NMR studies of phosphoric acid activated carbons, Carbon 46 (2008) 2113.

[42] A.M. Puziy, O.I. Poddubnaya, A. Martínez-Alonso, F. Suárez-García, J.M.D. Tascón, Synthetic carbons activated with phosphoric acid I. Surface chemistry and ion binding properties, Carbon 40 (2002) 1493.

[43] A.M. Puziy, O.I. Poddubnaya, A. Martínez-Alonso, F. Suárez-García, J.M.D. Tascón, Synthetic carbons activated with phosphoric acid III. Carbons prepared in air, Carbon 41 (2003) 1181.

[44] M. Pelavin, D. Hendrickson, J. Hollander, W. Jolly, Phosphorus 2p electron binding energies. Correlation with extended Hueckel charges, J. Phys. Chem. 74 (1970) 1116.

[45] D.M. Barbaux Y., Le Maguer D., Gengembre L., Huchette D., and Grimblot J., Bulk and surface analysis of a Fe-P-O oxydehydrogenation catalyst, Appl. Catalysis A 90 (1992) 51.

[46] P. Shih, S. Yung, T. Chin, FTIR and XPS studies of P_2O_5–Na_2O–CuO glasses, J. Non-cryst. Solids 244 (1999) 211.

[47] A.G. Kannan, N.R. Choudhury, N.K. Dutta, Synthesis and characterization of methacrylate phospho-silicate hybrid for thin film applications, Polymer 48 (2007) 7078.

[48] S. Biniak, G. Szymański, J. Siedlewski, A. Światkowski, The characterization of activated carbons with oxygen and nitrogen surface groups, Carbon 35 (1997) 1799.

[49] J. Pels, F. Kapteijn, J. Moulijn, Q. Zhu, K. Thomas, Evolution of nitrogen functionalities in carbonaceous materials during pyrolysis, Carbon 33 (1995) 1641.

[50] S. Kelemen, M. Gorbaty, P. Kwiatek, Quantification of nitrogen forms in Argonne premium coals, Energ. Fuel. 8 (1994) 896.

[51] J. Robertson, C. Davis, Nitrogen doping of tetrahedral amorphous carbon, Diam. Relat. Mater. 4 (1995) 441.

[52] D. Hulicova-Jurcakova, E. Fiset, G.Q. Lu, T.J. Bandosz, Changes in surface chemistry of carbon materials upon electrochemical measurements and their effects on capacitance in acidic and neutral electrolytes, ChemSusChem 5 (2012) 2188.

[53] W.B. Perry, T.F. Schaaf, W.L. Jolly, X-ray photoelectron spectroscopic study of charge distributions in tetracovalent compounds of nitrogen and phosphorus, J. Am. Chem. Soc. 97 (1975) 4899.

[54] C. Wang, L. Sun, Y. Zhou, P. Wan, X. Zhang, J. Qiu, P/N co-doped microporous carbons from H3PO4-doped polyaniline by in situ activation for supercapacitors, Carbon 59 (2013) 537.

[55] O.F. Mohammed, D. Pines, J. Dreyer, E. Pines, E.T.J. Nibbering, Sequential proton transfer through water bridges in acid-base reactions, Science 310 (2005) 83.

[56] H. K. Song, H. Y. Hwang, K. H. Lee, L.H. Dao, The effect of pore size distribution on the frequency dispersion of porous electrodes, Electrochim. Acta 45 (2000) 2241.

[57] E.D. Pershina, V.E. Burda, K.A. Kazdobin, V.V. Kokhanenko, Identification of the sugars content in the production of champagne by the electrochemical impedance spectroscopy method, Surf. Eng. Appl. Electrochem. 49 (2013) 348.

[58] P.L. Taberna, P. Simon, J.F. Fauvarque, Electrochemical Characteristics and Impedance Spectroscopy Studies of Carbon-Carbon Supercapacitors, J. Electrochem. Soc. 150 (2003) A292.

[59] J. Chmiola, G. Yushin, R. Dash, Y. Gogotsi, Effect of pore size and surface area of carbide derived carbons on specific capacitance, J. Power Sources 158 (2006) 765.

[60] C.J.T. de Grotthuss, Sur la décomposition de l'eau et des corps qu'elle tient en dissolution à l'aide de l'électricité galvanique, Ann. Chim. 58 (1806) 54.

[61] D.W. McKee, Oxidation protection of carbon materials, in: P.A. Thrower (Ed.), Chem. Phys. Carbon, Marcel Dekker, Inc., New York, 1991, p. 173.

[62] J. Zhang, X. Liu, R. Blume, A. Zhang, R. Schlögl, D.S. Su, Surface-Modified Carbon Nanotubes Catalyze Oxidative Dehydrogenation of n-Butane, Science 322 (2008) 73.